

ATOMS: ALMA Three-millimeter Observations of Massive Star-forming regions - VI. Hierarchical fragmentation and gas dynamics in IRDC G034.43+00.24

Hong-Li Liu,^{*1} Anandmayee Tej,^{*2} Tie Liu,^{*3,4} Namitha Issac,² Anindya Saha,² Paul F. Goldsmith,⁵ Jun-Zhi Wang,^{3,6} Qizhou Zhang,⁷ Sheng-Li Qin,¹ Ke Wang,^{8,9} Shanghuo Li,¹⁰ Archana Soam,¹¹ Lokesh Dewangan,¹² Chang Won Lee,^{10,13} Pak-Shing Li,¹⁴ Xun-Chuan Liu,⁹ Yong Zhang,¹⁵ Zhiyuan Ren,¹⁶ Mika Juvela,¹⁷ Leonardo Bronfman,¹⁸ Yue-Fang Wu,^{9,8} Ken'ichi Tatematsu,¹⁹ Xi Chen,²⁰ Di Li,^{16,21,22} Amelia Stutz,^{23,24} Siju Zhang,⁸ L. Viktor Toth,²⁵ Qiu-Yi Luo,³ Feng-Wei Xu,^{8,9} Jinzeng Li,¹⁶ Rong Liu,¹⁶ Jianwen Zhou,¹⁶ Chao Zhang,²⁶ Mengyao Tang,¹ Chao Zhang,¹ Tapas Baug,²⁷ E. Mannfors,¹⁷ Eswaraiiah Chakali,^{16,28} Somnath Dutta,²⁹

Affiliations are listed at the end of the paper

4 November 2021

ABSTRACT

We present new 3 mm continuum and molecular lines observations from the ATOMS survey towards the massive protostellar clump, MM1, located in the filamentary infrared dark cloud (IRDC), G034.43+00.24 (G34). The lines observed are the tracers of either dense gas (e.g., HCO⁺/H¹³CO⁺ J=1–0) or outflows (e.g., CS J=2–1). The most complete picture to date of seven cores in MM1 is revealed by dust continuum emission. These cores are found to be gravitationally bound, with virial parameter, $\alpha_{\text{vir}} < 2$. At least four outflows are identified in MM1 with a total outflowing mass of $\sim 45 M_{\odot}$, and a total energy of 1×10^{47} ergs, typical of outflows from a B0-type star. Evidence of hierarchical fragmentation, where turbulence dominates over thermal pressure, is observed at both the cloud and the clump scales. This could be linked to the scale-dependent, dynamical mass inflow/accretion on clump and core scales. We therefore suggest that the G34 cloud could be undergoing a dynamical mass inflow/accretion process linked to the multi-scale fragmentation, which leads to the sequential formation of fragments of the initial cloud, clumps, and ultimately dense cores, the sites of star formation.

Key words: stars: formation - stars: kinematics and dynamics; ISM: individual objects: G034.43+00.24; ISM: clouds.

1 INTRODUCTION

High-mass stars ($M_{*} > 8 M_{\odot}$) are of great importance in many astrophysical processes ranging from the production and transfer of heavy elements via nucleosynthesis, to the structure and evolution of their host galaxies, and even to future star formation in their natal molecular clouds (e.g., Kennicutt 2005; Urquhart et al. 2013). However, high-mass star formation remains poorly understood due to the observational challenges stemming from the relatively large distances to young high-mass stars, their rarity, opaque surroundings, short lifetime, and the complicated, crowded cluster environment (e.g., Zinnecker & Yorke 2007; Tan et al. 2014; Motte, Bontemps, & Louvet 2018). High-mass stars are known to form mainly in clusters through hierarchical fragmentation. In both observations and theoretical treatments (e.g., Zhang et al. 2009; Wang et al. 2011; Peretto et al. 2013; Wang et al. 2014; Beuther et al. 2018; Yuan et al. 2018; Motte, Bontemps, & Louvet 2018; Vázquez-Semadeni et al. 2019), hierarchical fragmentation has been observed to proceed on almost all scales from cloud, through filaments and clumps, to indi-

vidual star-forming cores¹, ultimately leading to a cluster of young stars. Moreover, the entire fragmentation process has been recognized to play a crucial role in determining the final mass of the individual stars formed, and thus the initial mass function, where the latter is a key input to the current theories.

Several efforts have been made to investigate the process of fragmentation, especially on clump and core scales (e.g., Palau et al. 2013, 2014; Csengeri et al. 2017; Beuther et al. 2018; Svoboda et al. 2019; Sanhueza et al. 2019; Li et al. 2019, 2020; Palau et al. 2021). However, finding different degrees of fragmentation makes it difficult to draw a decisive conclusion about the modality of fragmentation, which is a key parameter, especially for high-mass star formation. For example, Csengeri et al. (2017) found a low level of fragmentation with fragment masses above $40 M_{\odot}$ in their ALMA-880 μm (i.e., 340.1 GHz) observations of 35 massive clumps down

¹ The nomenclature of Zhang et al. (2009) and Wang et al. (2011, 2014) is adopted where a cloud is referred to as a structure of > 1 pc size, a clump as a structure of ~ 1 pc size, and a core as a structure of ~ 0.1 pc size. A core does not necessarily collapse into a single star but can fragment into substructures (a.k.a., condensations) and form a small cluster of stars.

* E-mail: hongliliu2012@gmail.com, liutie@shao.ac.cn, and tej@iist.ac.in

to 0.06 pc scale. In contrast, based on ALMA-1 mm observations towards 12 infrared dark cloud (IRDC) clumps, [Sanhueza et al. \(2019\)](#) revealed a higher level of fragmentation with a large population of low-mass ($\leq 1 M_{\odot}$) cores of sizes ≤ 0.1 pc but no high-mass counterparts ($\geq 30 M_{\odot}$). These different degrees of fragmentation probably represent different modalities that control the mass reservoir feeding the individual stars, as predicted by the two main competing theories of high-mass star formation: “core-accretion” ([McKee & Tan 2003](#)) and “competitive-accretion” ([Bonnell, Vine, & Bate 2004](#)). The core-accretion hypothesis, which is essentially a scaled-up version of low-mass star formation, favors the fragmentation of a clump into massive cores that proceed to form high-mass stars. In comparison, the competitive-accretion theory predicts the fragmentation of a clump into a larger population of low-mass cores that competitively accrete from the common mass reservoir. In this framework, cores located at the gravitational well of the system preferentially form high-mass stars. Therefore, more detailed investigation is still needed to establish the link between the observations of the degree of fragmentation and theoretical predictions.

Fragmentation tends to be associated with rich and complex kinematics and dynamics as a result of the interaction among gravity, turbulence, magnetic fields, and/or other factors such as intense radiative feedback from newly-formed stars. Both kinematics and dynamics are therefore thought to be useful probes for dissecting the underlying physics (e.g. mass accretion, outflows) related to hierarchical, multi-scale fragmentation processes in star formation. Recent state-of-the-art numerical simulations of cloud complexes (e.g., [Padoan et al. 2020](#)) have reproduced a web of filamentary structures, each with longitudinal velocity gradient indicative of a mass flow along the filament converging towards the web node, where high-mass young stellar objects (YSOs) are preferentially found to reside. The mass of the final stars has therefore been suggested to be regulated not only by the clump- or core-scale mass accretion but also by the larger-scale mass inflow/accretion. In fact, this multi-scale mass inflow/accretion has been revealed in previous multi-scale kinematic observations ([Zhang & Wang 2011](#); [Peretto et al. 2013](#); [Chen et al. 2017](#); [Yuan et al. 2018](#)). For example, in their study of the high-mass protostellar clump, G22, [Yuan et al. \(2018\)](#) observed that the protostar grows in mass simultaneously via core, clump, and cloud-fed accretion with an increasing trend of mass inflow/infall rates of $7.4 \times 10^{-5} M_{\odot} \text{yr}^{-1}$, $7.2 \times 10^{-4} M_{\odot} \text{yr}^{-1}$, and $\sim 100 M_{\odot} \text{yr}^{-1}$, respectively. It thus appears extremely promising to conduct similar studies to obtain an in-depth understanding of the kinematics and dynamics involved in the process of multi-scale fragmentation associated with high-mass star formation.

The primary target for this study is the massive clump, MM1, located in the well-known filamentary IRDC, G034.43+00.24 (hereafter G34 [Rathborne et al. 2005](#); [Rathborne, Jackson, & Simon 2006](#); [Lu et al. 2014](#); [Liu et al. 2020a](#)). We have also probed another associated massive clump, MM2, which is partly covered with the ATOMS survey. We adopt a kinematic distance of 3.7 ± 0.3 kpc (e.g., [Rathborne et al. 2005](#); [Xu et al. 2016](#); [Tang et al. 2019](#); [Liu et al. 2020a](#)) to this cloud. The two massive clumps have a few hundred solar masses within diameters of 0.2–0.5 pc. MM1 has a bolometric luminosity of $2.4 \times 10^4 L_{\odot}$ mainly due to an associated B0-type YSO (Fig. 1), while MM2 has a bolometric luminosity of $1.4 \times 10^4 L_{\odot}$ mainly from an associated ultra-compact HII region (UC-HII, i.e., IRAS 18507+0121, [Bronfman, Nyman, & May 1996](#)). The coexistence of these star-forming signatures and the IRDC nature of the G34 cloud suggests early stages of high-mass star formation in the clumps, MM1 and MM2.

In this paper, we present our new ALMA 3 mm observations to-

wards IRDC G34, which is part of the ATOMS survey² (Project ID: 2019.1.00685.S, [Liu et al. 2020b,c, 2021](#), hereafter Paper I, Paper II, and Paper III, respectively, see Sect. 2). The ATOMS survey is aimed to investigate statistically the relation between high-mass star formation and the distribution of dense gas, filamentary structures, and feedback, by observing 3 mm continuum and gas emission at a nearly uniform angular resolution of $\sim 2''$ towards a sample of 146 high-mass star-forming IRAS regions in the range $-80^{\circ} < l < 40^{\circ}$ and $|b| < 2^{\circ}$ ([Bronfman, Nyman, & May 1996](#); [Faúndez et al. 2004](#)). The overview paper (Paper I) presents the source sample, the spectral setup, and the major goals of the survey. Paper II addresses the relation between high-mass star formation and the dense gas distribution by investigating the star formation scaling relations inferred from different dense gas tracers (e.g., $\text{HCO}^+/\text{H}^{13}\text{CO}^+$, $\text{HCN}/\text{H}^{13}\text{CN}$). Paper III includes the catalogues of candidate hot molecular cores and hyper/ultra compact HII regions, which provide an important foundation for future studies of the early stages of high-mass star formation across the Milky Way.

In the present paper, we make full use of the ATOMS data to gain insight into the fragmentation and dynamical processes of the G34 cloud through observations of its two massive, luminous protostellar clumps, MM1 and MM2. The paper is organized as follows: Section 2 gives a brief description of the ALMA observations of the ATOMS survey. Section 3 presents analysis of the ATOMS data, Section 4 discusses the observed hierarchical fragmentation and the associated dynamical mass inflow/accretion scenario, and Section 5 summarizes the results.

2 ALMA OBSERVATIONS AND DATA REDUCTION

Observations of the ATOMS survey consist of single pointings towards 146 IRAS clumps by both the Atacama Compact 7-m Array (ACA; Morita Array) and the 12-m array (C43-2 or C43-3 configurations) in Band 3. Eight spectral windows (SPWs) were optimised to cover 11 commonly-used lines that includes the tracers of dense gas (e.g., $\text{HCO}^+/\text{H}^{13}\text{CO}^+$), hot molecular core gas (e.g., CH_3OH), shocked gas (e.g., SiO, and SO), and ionized gas (e.g., $\text{H}40\alpha$). The basic parameters (e.g., rest frequency, transition) of these lines are listed in Table 2 of Paper I. The SPWs 1–6 are located at the lower sideband in the range [86.31, 99.40] GHz with spectral resolution of $\sim 0.2 - 0.4 \text{ km s}^{-1}$ for kinematic measurements, while SPWs 7–8 in the upper sideband in the range [99.46, 101.34] GHz each has a broad bandwidth of 1875 MHz at a spectral resolution of $\sim 1.6 \text{ km s}^{-1}$ for sensitive continuum measurements.

The data were calibrated in CASA 5.6 ([McMullin et al. 2007](#)). We then imaged and cleaned the ACA and 12 m-array data jointly using natural weighting (to optimise the signal-to-noise ratio) and taking $p_{\text{limit}} = 0.2$, in the CASA *tclean* task, for both continuum images and line cubes. Continuum images were created from line-free frequency ranges of SPWs 7–8 centred at ~ 99.4 GHz while the spectral line cube of each SPW was produced with its native spectral resolution. The resulting continuum image and line cubes for the 146 target clumps have angular resolutions $\sim 1''.2-1''.9$, and maximum recoverable angular scales $\sim 60''$.

In this paper, we analyze the I18507+0121 source from the ATOMS, whose ALMA observations cover the MM1 and MM2 clumps of G34. The analysis presented is carried out on the combined data sets unless specified otherwise. The 12m+ACA combined

² ATOMS: ALMA Three-millimeter Observations of Massive Star-forming regions survey

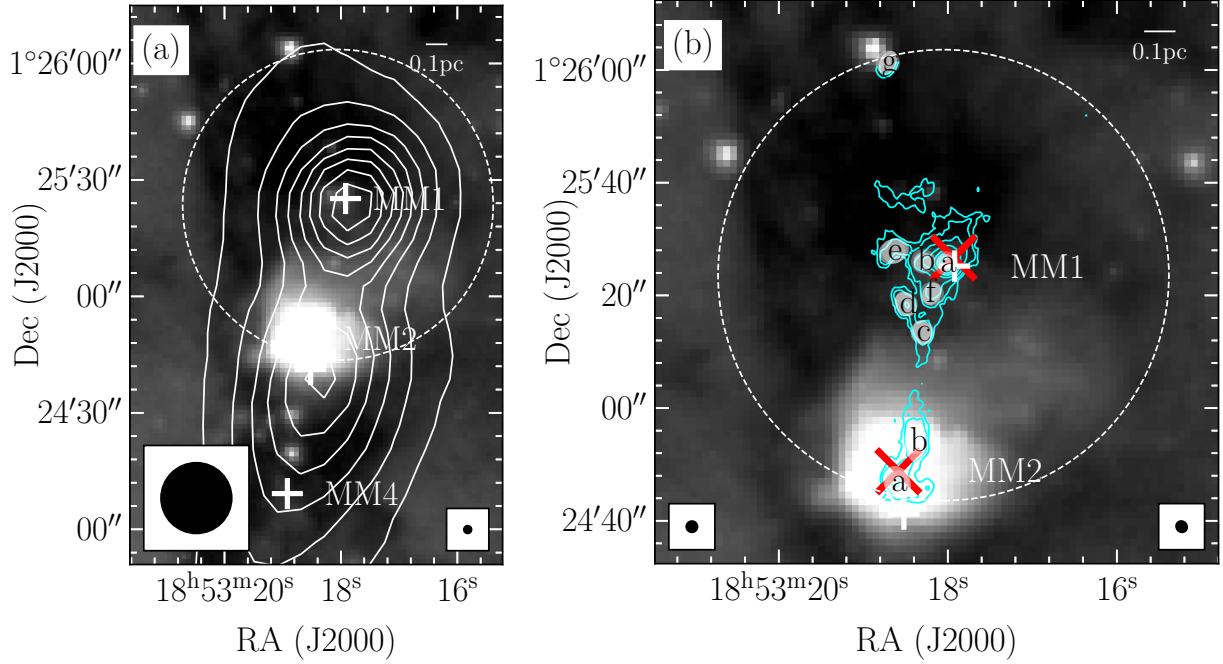


Figure 1. (a) The two massive protostellar clumps, MM1 and MM2, of IRDC G34 in *Spitzer* 8.0 μm image overlaid with the ATLASGAL 870 μm continuum contours. The contours start at 3 rms (rms $\sim 0.6 \text{ Jy beam}^{-1}$) increasing in steps following the power-law $D = 3 \times N^p + 2$, where D is the dynamical range of the intensity map (i.e., the ratio between the peak and the rms noise), N is the number of contours used (8 in this case). The millimeter clumps identified from the 1.2 mm continuum maps presented by Rathborne, Jackson, & Simon (2006) are indicated with plus symbols. The beams of the 8.0 μm and 870 μm data are shown at the bottom left, and bottom right corners, respectively. (b) Close-up view of MM1 and MM2. The contours represent the ATOMS 3 mm continuum emission. Note that the ATOMS map is not corrected for the primary beam. The contour levels start at 3 rms (rms $\sim 0.3 \text{ mJy beam}^{-1}$) with steps following the same power-law form as in panel (a). Labels a–g identify the cores extracted from the continuum emission. The beams of the 8.0 μm and 3 mm data are shown at the bottom left, and bottom right corners, respectively. The locations of the B2-type YSO associated with MM1 and the UC-HII region associated with MM2 are indicated with red X symbols. The dashed circle in both panels demarcates the field view of the ATOMS 3 mm observations.

continuum image of this source has a beam size of $1.9'' \times 2.1''$, and a sensitivity of $1 \text{ rms} = 0.3 \text{ mJy beam}^{-1}$, which corresponds to a mass sensitivity of $\sim 0.1 M_{\odot}$ at the distance of the source for a dust temperature of $\sim 20 \text{ K}$ (see Sect. 3.1 for the detailed mass calculation). For line cubes, only the HCO^+ (1–0), H^{13}CO^+ (1–0), SiO (2–1), SO (3–2), CS (2–1), and CH_3OH $2_{(1,1)}-1_{(1,0)}\text{A}$ lines are utilized for investigating the kinematics and dynamics of MM1 and MM2. The velocity resolutions for the HCO^+ , H^{13}CO^+ / SiO , and $\text{SO}/\text{CS}/\text{CH}_3\text{OH}$ lines are 0.1, 0.2, and 1.5 km s^{-1} , respectively, and the sensitivity levels are ~ 12 , 8, and 3 mJy beam^{-1} , respectively.

3 RESULTS AND ANALYSIS

3.1 3 mm continuum emission

Figure 1 illustrates the overall morphology and location of the MM1 and MM2 protostellar clumps of G34 in the *Spitzer* 8.0 μm image overlaid with ATLASGAL 870 μm dust continuum in panel (a), and with the ATOMS 3 mm continuum data in panel (b). The ATOMS continuum image presented in this figure and Fig. 2 is not corrected for the primary beam response. This is done only for the purpose of display since it enables a uniform noise level to be shown in the map. But for the analysis of the core properties, the primary-beam corrected 3 mm image is used (see Paper III for more details). The dashed circle in Fig. 1 marks the field of view ($80''$ in diameter) of the resulting combined image of ATOMS used in this study. As seen, the MM1 clump is fully covered while only half of the MM2 area is

observed by the ATOMS. The large-scale filamentary cloud overall appears dark against the background emission at $8 \mu\text{m}$. Also marked in the figure is the chain of the three millimeter clumps (i.e., MM1, MM2, and MM4) identified by Rathborne, Jackson, & Simon 2006 from 1.2 mm continuum observations. The orientation of the clumps along the filament is seen to be replicated on smaller scales as well, as is evident from the north-south spread of the detected cores in the 3 mm continuum of the ATOMS data. The 3 mm continuum emission observed across the entire region mainly comes from thermal dust emission since ATOMS detected no $\text{H}40_{\alpha}$ emission. Further, only two very compact centimetre sources of size $\sim 1''$ are detected by Rosero et al. (2016), which are confined within the centres of the MM1 and MM2 clumps.

The high angular resolution of the ATOMS 3 mm continuum map allows to identify the dense cores where stars form. Paper III adopted a combination of the *Dendrogram* algorithm and *CASA-imfit* function to extract cores. As discussed by these authors, the former technique does not always provide good measurements of the core parameters on size and position angle, while the latter performs better in this regard through a two-dimensional Gaussian fit to the emission. Following this approach, nine cores are extracted from the 3 mm continuum map with seven (i.e., MM1a–g, see Fig. 1b) in MM1 and two (i.e., MM2a–b) belonging to MM2. Note that the MM1-b core was manually located and then extracted with *CASA-imfit* since it was not automatically detected by *Dendrogram* due to its close proximity and small intensity contrast relative to the neighbouring MM1-a core. The additional extraction of MM1-b was

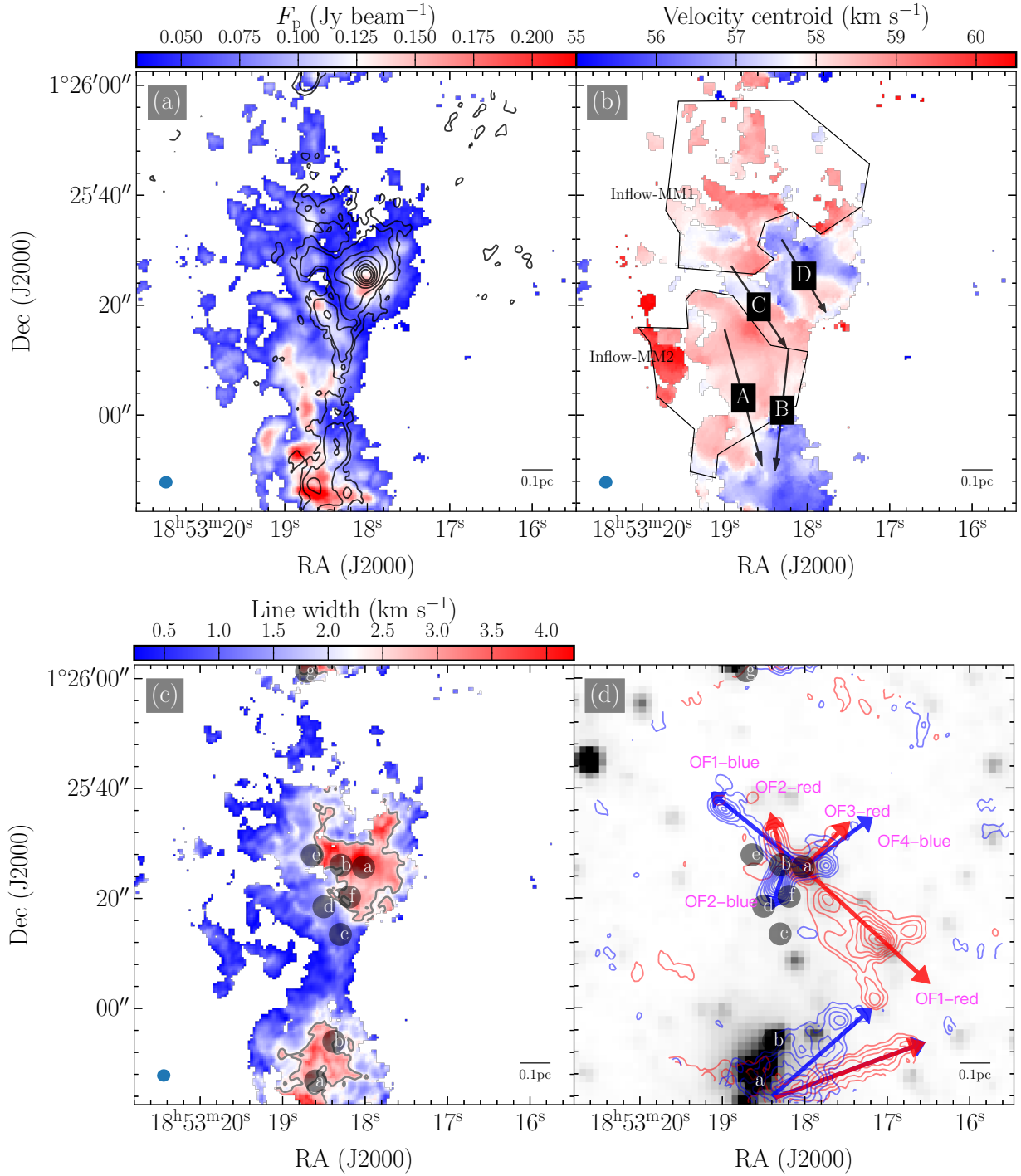


Figure 2. (a) Peak intensity map of H^{13}CO^+ (1-0) for the MM1 and MM2 protostellar clumps in G34. The 3 mm dust continuum emission is shown in black contours, starting at 3 rms ($\text{rms} \sim 0.3 \text{ mJy beam}^{-1}$) with the steps following the same power-law form as in Fig. 1. (b) Moment 1 map of H^{13}CO^+ (1-0). The arrows A–D mark the directions of the observed velocity-coherent gradients. The polygons represent the gas inflow regions for each cluster of cores in MM1 and MM2. (c) Line width map of H^{13}CO^+ (1-0). The contour represents a line width of 2.5 km s^{-1} . (d) CS (2-1) outflows (contours) superimposed on the Spitzer $4.5 \mu\text{m}$ image. The red and blue arrows indicate the red and blue lobes of outflows, respectively. Labels a–g in panels (c) and (d) identify the dense cores in MM1 and MM2 protostellar clumps. In all panels, the map is displayed only at the positions where the peak intensity of the spectrum is ≥ 5 times the local noise level.

Table 1. Continuum core parameters.

Name	RA (J2000)	Dec. (J2000)	$FWHM_{\text{dec}}$ maj('') \times min('')	PA deg	$F_{3\text{mm}}^{\text{int.}}$ mJy	$F_{3\text{mm}}^{\text{p}}$ mJy beam $^{-1}$	R_{core} 10^{-2} pc	T_{gas} K	M_{core} M_{\odot}	$\log(n_{\text{core}})$ cm $^{-3}$	Σ_{core} g cm $^{-2}$	V_{lsr} km s $^{-1}$	ΔV km s $^{-1}$	α_{vir}
MM1-a	18:53:18.02	1:25:25.7	2.3 \times 2.2	21.4	124.2 \pm 0.8	54.7 \pm 0.2	2.0 \pm 0.2	100.0	199 \pm 32	7.4	32.7	57.6 \pm 0.2	4.5 \pm 0.2	0.5
MM1-b	18:53:18.29	1:25:25.9	2.2 \times 2.0	102.1	9.6 \pm 0.1	9.6 \pm 0.2	1.9 \pm 0.2	27.6	58 \pm 9	7.3	11.0	57.1 \pm 0.2	2.9 \pm 0.2	0.6
MM1-c	18:53:18.30	1:25:13.6	3.5 \times 2.4	16.0	9.1 \pm 1.0	2.8 \pm 0.2	2.6 \pm 0.2	14.2	115 \pm 19	7.0	11.1	59.3 \pm 0.2	1.1 \pm 0.2	0.1
MM1-d	18:53:18.50	1:25:18.4	3.8 \times 2.5	32.0	10.3 \pm 1.0	3.0 \pm 0.2	2.7 \pm 0.2	13.8	136 \pm 22	7.0	12.1	58.6 \pm 0.2	1.8 \pm 0.2	0.1
MM1-e	18:53:18.64	1:25:28.0	4.5 \times 3.5	112.9	5.6 \pm 0.1	1.9 \pm 0.2	3.5 \pm 0.3	22.6	42 \pm 7	6.5	2.2	57.4 \pm 0.2	1.6 \pm 0.2	0.5
MM1-f	18:53:18.19	1:25:20.3	2.7 \times 2.1	152.5	6.9 \pm 0.1	5.5 \pm 0.2	2.1 \pm 0.2	18.6	65 \pm 11	7.2	9.5	56.9 \pm 0.2	3.3 \pm 0.2	0.8
MM1-g	18:53:18.71	1:26:1.3	3.7 \times 1.6	151.0	24.5 \pm 0.9	9.1 \pm 0.2	2.1 \pm 0.2	21.7	196 \pm 32	7.4	28.3	58.4 \pm 0.2	3.4 \pm 0.2	0.3
MM2-a	18:53:18.60	1:24:46.7	5.3 \times 4.0	23.2	62.3 \pm 1.5	9.8 \pm 0.2	4.1 \pm 0.3	100.0	97 \pm 16	6.4	3.8	56.5 \pm 0.2	2.5 \pm 0.2	0.7
MM2-b	18:53:18.38	1:24:54.1	6.7 \times 2.9	0.8	34.0 \pm 1.4	5.5 \pm 0.2	3.9 \pm 0.3	20.8	281 \pm 46	6.9	12.2	56.2 \pm 0.2	2.7 \pm 0.2	0.2

Note: R_{core} is derived from $R_{\text{eff}}/3600 \times \pi/180 \times D$ given the relation $R_{\text{eff}} = \sqrt{FWHM_{\text{dec}}^{\text{maj}} \times FWHM_{\text{dec}}^{\text{min}}}/2$, and the distance D of the core. Gas temperature for all the cores, except for MM1-a and MM2-a, is estimated from the kinetic temperature map obtained from VLA observations of NH_3 by Lu et al. (2014). For cores MM1-a and MM2-a, the temperature is assumed to be 100 K given their association with a hot molecular core and an UC-HII region, respectively. V_{lsr} and ΔV along with the associated errors are derived from single Gaussian component fit to the average spectrum of H^{13}CO^+ (1–0) over each core. The errors for the fluxes result from the 2D Gaussian fitting in the core extraction, while the ones for R_{core} , M_{core} , and n_{core} are mainly due to the distance uncertainty.

driven by the associated outflows (see Fig. 2d). Its existence was further verified through a careful visual examination of the radial intensity profile along the direction connecting both MM1-b and MM1-a sources, where the weak and strong intensity peak components correspond to the two sources, respectively.

Overall, the result of core extraction in this work matches that of Paper III with the exception of the two cores, MM1-g, and MM2-a. Both of them are located outside a circle of radius 36'' around the image centre, which was imposed as a mask for batch extraction of cores from all of the 146 ATOMS clumps, and thus ignored in Paper III. Our ATOMS observations have revealed the most complete population of cores (i.e., a cluster of seven cores) in MM1, compared with the previous SMA observations (e.g., Rathborne et al. 2011), in which only the MM1-a core was revealed. This could be a consequence of either the missing-flux effect due to the limited uv coverage by SMA or the poor sensitivity. Additionally, due to the incomplete coverage by the ATOMS for MM2, we believe that the population of cores in this clump has not been fully unveiled, and this clump could also be harbouring a cluster of cores.

The measured parameters of the nine cores are listed in Table 1, including the deconvolved sizes of the major and minor axes (Col. 4), the position angle (Col. 5), the core-integrated 3 mm flux (Col. 6), and the core-peak flux (Col. 7). Note that both MM1-a and MM2-a cores have an associated compact centimeter source, each with a size of $\sim 1''$. The two sources coincide with an early B-type star in MM1 (see Fig. 1, Shepherd et al. 2007), and an UC-HII region in MM2. In addition, the centimeter sources in MM1-a and MM2-a correspond to partially optically-thick free-free emission and non-thermal emission, respectively, with the former having a spectral index of $\alpha = 0.7$ in the frequency range 4.9 GHz to 25.5 GHz and the latter having $\alpha = -0.5$ (Rosero et al. 2016). Given a total flux density of ~ 0.4 mJy and 9.5 mJy at 4.9 GHz for the centimeter sources in MM1-a, and MM2-a, respectively, the relation $S_{\nu} \propto \nu^{\alpha}$ yields a flux density of ~ 3 mJy and 2.1 mJy, respectively, at 3 mm, which is negligible compared to the total fluxes of the two cores.

The mass, M_{core} , and the column density, N_{core} , of the cores were calculated following Eqs. B1–B2 of Paper III. In the calculation, the gas temperature for all the cores, except for MM1-a and MM2-a, is estimated from the kinetic temperature map obtained from the VLA 3''-resolution observations of the NH_3 (1, 1) and (2, 2) inversion lines by Lu et al. (2014). For MM1-a and MM2-a, the temperature is assumed to be 100 K due to the presence of an associated hot molecular core, and an UC-HII region (Rathborne et al. 2011, Paper III), respectively. In addition, a gas-to-dust mass ratio of $R_{\text{gd}} = 100$ was

adopted. Recent works propose higher values (R'_{gd}) like 150 (Draine 2011) or 162 (Peters et al. 2017). One can estimate M_{core} and N_{core} with different gas-to-dust mass ratios simply by multiplying a scaling factor of $R'_{\text{gd}}/R_{\text{gd}}$. In the above calculation the core flux includes background emission, which could lead to the overestimation of the core masses. In practice, the background emission is difficult to be accurately subtracted especially from the high-resolution ATOMS data that has already filtered out a significant portion of large-scale components. For a conservative estimate, we assume a constant value of 1 rms level for the background emission. Using this, it is seen that the median value of the new core masses decreases by $\sim 25\%$ where the decrease in mass is mostly seen in the relatively low-density cores while the more massive and dense ones remain more or less unchanged.

Furthermore, the mass surface density can be derived from $\Sigma_{\text{core}} = M_{\text{core}}/(\pi R_{\text{core}}^2)$, while the number density from $n_{\text{core}} = N_{\text{core}}/2R_{\text{core}}$, where R_{core} is the core radius equal to the geometric mean of $FWHM_{\text{dec}}^{\text{maj}}$ and $FWHM_{\text{dec}}^{\text{min}}$ at the core distance. The above derived parameters can be found in Cols. 9–11 of Table 1. In summary, we find $R_{\text{core}} \sim 0.02$ – 0.04 pc with a median value of 0.03 pc, $M_{\text{core}} \sim 42$ – $281 M_{\odot}$ with a median value of $115 M_{\odot}$, $n_{\text{core}} \sim 0.2 \times 10^7$ – 2.8×10^7 cm $^{-3}$ with a median value of 1.1×10^7 cm $^{-3}$, and $\Sigma_{\text{core}} \sim 2$ – 32 g cm $^{-2}$ with a median value of 11 g cm $^{-2}$. If a theoretical threshold of 1 g cm $^{-2}$ above which the cores most likely form high-mass stars, is assumed (Krumholz & McKee 2008), then the entire population of cores detected in this study have the ability to form high-mass stars.

Following the method described above, we also estimated the mass, M_{cl} , and the number density, n_{cl} , of the G34 cloud (80'' in size) considering the region within the field of view of the ATOMS observations. Since the kinetic temperature map of Lu et al. (2014) is obtained using interferometric observations, structures with spatial scales larger than that of the ATOMS cores are resolved out. Hence, for these calculations, we assume a cloud-average dust temperature of ~ 21 K, which was measured over the field of view of the ATOMS observations from the publicly available dust temperature map created using the point processing mapping (PPMAP) technique, a state-of-the-art spectral energy distribution fit method (Marsh et al. 2017). The assumption of this temperature is in good agreement with the cold nature of the IRDC cloud (e.g., Carey et al. 1998, 2000; Rathborne, Jackson, & Simon 2006; Soam et al. 2019). Taking the integrated flux of 480 Jy at 870 μm from the ATLASGAL image of the cloud leads to $M_{\text{cl}} \sim 4.2 \times 10^4 M_{\odot}$, and $n_{\text{cl}} \sim 2.6 \times 10^5$ cm $^{-3}$. The mass conversion efficiency from cloud

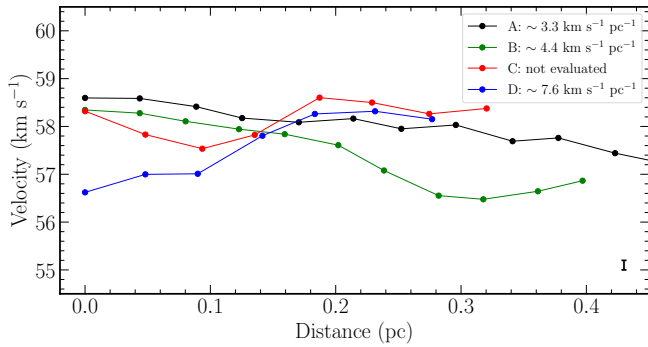


Figure 3. Velocity distribution derived from H^{13}CO^+ (1–0) along the four selected directions A–D, which are indicated in Fig. 2b. The typical error bar of the velocity gradient is shown at the bottom right.

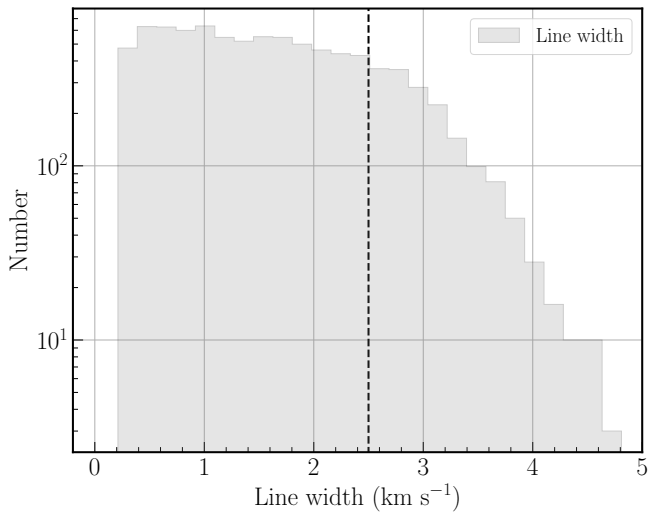


Figure 4. Distribution of the line widths derived from H^{13}CO^+ (1–0). The y-axis shows the number of pixels. An inflection in the distribution can be found at $\sim 2.5 \text{ km s}^{-1}$ (indicated by the dashed vertical line).

to cores is rather low at about 3%, although the masses of the cores are far above the mass sensitivity (i.e., $\sim 0.3 M_{\odot}$ for a 3 rms detection) of the observations, implying that most of the cloud gas is not efficiently transformed into cores.

3.2 Molecular gas emission

The average spectrum of H^{13}CO^+ (1–0) over the entire region investigated here reveals a systemic velocity of $V_{\text{lsr}} = 57.6 \text{ km s}^{-1}$. In general, H^{13}CO^+ emission is treated as relatively optically thin. However, this may not be the case for the densest part of cores. Following Eq. 1 of Liu et al. (2020a), we calculate the optical thickness from the peak intensity of H^{13}CO^+ of the nine cores with the assumptions of local thermodynamic equilibrium (LTE). This yields optical depth values in the range of 0.04 – 0.39 and hence supports the optically thin assumption for the H^{13}CO^+ emission. Besides, extended emission of H^{13}CO^+ appears as a single-peaked spectral profile across the entire region at a high spectral resolution 0.2 km s^{-1} , which makes the H^{13}CO^+ (1–0) line a good probe for the spatial distribution of molecular gas within the MM1 and MM2 clumps.

Figure 2a displays the map of the peak intensity of H^{13}CO^+ (1–0). For comparison, the 3 mm dust continuum is also overlaid as contours in the figure. H^{13}CO^+ (1–0) gas and 3 mm dust continuum distribution are found to match each other well in dense regions, with the former being much more extended than the latter across the entire region. In particular, a bright branch of H^{13}CO^+ emission, which appears to stretch towards the cluster of cores (MM2a–b) in MM2, does not have detectable continuum emission at the current sensitivity. The nondetection of dust continuum indicates that this branch of H^{13}CO^+ emission could be ambient gas having lower column density than that concentrated in the clusters of cores with apparent dust emission.

Figure 2b presents the moment 1 map of H^{13}CO^+ (1–0) that can reveal the global velocity field. Velocity gradients can be seen towards the cluster of cores in both MM1 and MM2. In particular, the velocity gradients towards the cluster of cores in MM2 appear to match the bright branch of H^{13}CO^+ gas emission mentioned above, suggesting that ambient gas is being accelerated by the gravity of the cluster of cores in MM2, and thus inflowing towards them (see Sect. 4.2 for additional discussion). Quantitatively, the velocity gradients are evaluated along the four directions (indicated by arrows A–D in Fig. 2b). We find from Fig. 3 that the gradients lie in the range of $\sim 3\text{--}8 \text{ km s}^{-1} \text{ pc}^{-1}$. Of particular interest is the gradient along the direction D, which appears to be the signature of rotational motion (see Sect. 3.5 for more analysis).

Figure 2c shows the line width map of H^{13}CO^+ (1–0) reflecting the global kinematics of the entire region investigated here. The line width tends to be enhanced around the centres of the clusters of cores in both MM1 and MM2. Given that the H^{13}CO^+ (1–0) emission is seen to be optically thin, the effect of optical depth can be ruled out and this enhancement can be attributed to intense star-forming feedback (e.g., energetic outflows and stellar winds) due to the presence of the luminous YSO in MM1 and the UC-HII region in MM2 (Shepherd et al. 2007; Liu et al. 2020a). Moreover, the dynamical motions of the gravity/turbulence-driven inflows toward the centres of MM1 and MM2 can be an additional source for the enhanced line width.

To quantitatively describe this enhancement, we plot, in Fig. 4, the distribution of the line widths for the entire region. A distinct inflection at the line width of $\sim 2.5 \text{ km s}^{-1}$ is evident on visual inspection of the distribution. This turnover could represent the threshold above which the line width is enhanced by strong feedback from star formation and probably by the dynamical gas inflows, and below which the gas kinematics are less affected. This threshold can also be found in Fig. 2c where the threshold of $\sim 2.5 \text{ km s}^{-1}$ (in gray contour) does separate the weak- and strong-feedback areas well. The mean line width is $\sim 2.9 \text{ km s}^{-1}$ in the area of strong feedback, and $\sim 1.3 \text{ km s}^{-1}$ elsewhere.

3.3 Molecular outflows

Previous single-dish as well as interferometric observations have shown the presence of outflows in the MM1 and MM2 clumps (e.g., Rathborne et al. 2011; Zhang et al. 2014; Liu et al. 2020a). With the new observations from the ATOMS survey that include several commonly-used outflow tracers like HCO^+ , CS, SiO, SO, and CH_3OH , we identify, in different tracers, the outflows associated with the two clusters of cores in MM1 and MM2. In the identification, the outflowing gas velocities of each tracer (line) are taken from the line wings of its spectrum, which lie outside the full width of half maximum of the spectrum. The spectrum used is averaged

Table 2. CS (2-1) outflow parameters.

Outflow	Lobes	$\langle L \rangle$ pc	$\langle V \rangle$ km s ⁻¹	M_{out} M_{\odot}	P_{out} $10^2 M_{\odot}$ km s ⁻¹	E_{out} 10^{46} erg	F_{out} $10^{-3} M_{\odot}$ km s ⁻¹ yr ⁻¹	t_{dyn} 10^3 yr	\dot{M}_{acc} $10^{-5} M_{\odot}$ yr ⁻¹
MM1-OF1	B+R	0.47 ± 0.07	14.6 ± 1.5	34.9 ± 1.7	5.1 ± 0.3	7.8 ± 0.4	16.2 ± 5.0	3.1 ± 0.8	3.0 – 6.0
MM1-OF2	B+R	0.18 ± 0.03	14.9 ± 1.5	8.0 ± 0.4	1.2 ± 0.1	1.8 ± 0.1	10.1 ± 3.3	1.2 ± 0.3	2.0 – 4.0
MM1-OF3	R	0.23 ± 0.02	18.2 ± 1.8	1.8 ± 0.1	0.3 ± 0.1	0.6 ± 0.1	2.6 ± 0.6	1.3 ± 0.2	0.4 – 0.7
MM1-OF4	B	0.14 ± 0.01	12.0 ± 1.2	1.1 ± 0.1	0.1 ± 0.1	0.2 ± 0.1	1.1 ± 0.3	1.2 ± 0.2	0.2 – 0.3
Total	–	–	–	44.7 ± 1.7	6.6 ± 0.3	10.2 ± 0.4	29.0 ± 5.0	–	5.4 – 10.7

Note: B and R in Col. 2 stand for the blue and red lobe of outflows, respectively.

over the entire region investigated here. The blue- and red-shifted outflowing gas emission, in sequence, is integrated over the velocity ranges (1) [44.0, 55.0] km s⁻¹ and [60.0, 76.0] km s⁻¹ for HCO⁺ (1-0), (2) [40.0, 51.4] km s⁻¹ and [63.4, 82.0] km s⁻¹ for CS, (3) [42.0, 51.3] km s⁻¹ and [63.5, 74.0] km s⁻¹ for SiO, (4) [42.0, 52.7] km s⁻¹ and [62.2, 78.0] km s⁻¹ for SO, and (5) [46.0, 54.2] km s⁻¹ and [60.6, 66.0] km s⁻¹ for CH₃OH.

In total, six outflows are identified with four within the MM1 clump (i.e., MM1-OF1 to MM1-OF4) and two within MM2. All of the outflows are identifiable in the five tracers with the exception of MM1-OF3, which is visible only in CS and SiO emission. The outflows identified with each tracer are plotted in Figs. 2d and A1. For comparison, the *Spitzer* 4.5 μ m is overlaid, which is thought to be an indicator of shocked gas. As seen, the outflow gas extent does not correspond to the extended 4.5 μ m emission well. From the figure, MM1-OF1/OF3/OF4 appear to be driven by the embedded source(s) in MM1-a while MM1-OF2 by the source(s) in MM1-b. In MM1, all of the outflows except for MM1-OF1 are distinct from the results of Shepherd et al. (2007). The low-resolution (angular resolution of 3''6) CO (1-0) observations presented by these authors do not reveal the presence of MM1-OF2 nor do they distinguish between the MM1-OF3 and MM1-OF4 outflows. Although both MM1-OF3 and MM1-OF4 outflows display single lobes, these have a high possibility of being associated with the MM1-a core due to the outflowing velocities ranging around the systemic velocity of MM1-a.

In a later study by Isequilla et al. (2021), based on higher 0''8-resolution observations of CO (2-1), the two lobes of MM1-OF2 were reported as separate outflows but not as a bipolar outflow. Since the driving source(s) of the outflows within MM2 (i.e., MM2-OF1/OF2) could not be probed due to the incomplete coverage of ATOMS, they are not considered for further analysis. In addition, we find that the outflows identified with the new observations are more collimated than those seen from the CO (1-0) observations by Shepherd et al. (2007), suggesting that the outflow tracers used here, that have much higher critical density than CO (1-0), could be probing the compact, highly-collimated jets.

3.4 Outflow parameters in MM1

Parameters such as the momentum, dynamical age, and ejection rate are valuable for characterizing the outflows. In principle, both CS and SiO emission can be used for the calculation since from Figs. 2d and A1 they both are found to trace the extent of all of the outflows better than the other three tracers. Since the shock-sensitive SiO is preferentially enhanced in shocked regions, and less abundant elsewhere, the core-scale abundance is required to more properly estimate the abundance-related parameters like the momentum. Since no core-scale measurement of SiO abundance is available for the cluster of cores in MM1, we consider CS emission only, which can

be abundant in non-shocked as well as shocked regions, and in general is not as sensitive to shocked gas as SiO emission.

Following Shepherd et al. (2007), an inclination angle of 45° was assumed for simplicity, which minimizes the errors introduced by inclination effects for outflows with unknown orientation. The total outflowing gas mass, M_{out} , was inferred from ΣM_i , where the gas mass, M_i , in the velocity channel i was calculated from Eq. 4 of Liu et al. (2020a) assuming optically-thin emission, LTE conditions, and a CS abundance of 5.8×10^{-10} inferred by Liu et al. (2020a). In addition, the clump-average dust temperature of 38 K as quoted in Liu et al. (2020a) was taken as the excitation temperature in the calculation. The momentum, P_{out} , was derived from $\Sigma M_i v_i$ and the kinetic energy, E_{out} , from $\frac{1}{2} \Sigma M_i v_i^2$ with v_i defined as the central velocity of the i^{th} channel relative to V_{lsr} . The dynamical age, t_{dyn} , was estimated from $\langle L \rangle / \langle V \rangle$, where $\langle L \rangle$ is the average length of the red and/or blue lobes of outflows and $\langle V \rangle$ is the intensity-weighted mean velocity defined as $P_{\text{out}} / \Sigma M_i$. Accordingly, the outflowing mass rate, \dot{M}_{out} , is given by $\Sigma M_i / t_{\text{dyn}}$, and the mechanical force, F_{out} , by $P_{\text{out}} / t_{\text{dyn}}$.

Table 2 summarises the above-derived parameters for the CS outflows within MM1. The parameter errors mainly arise from the uncertainties of the distance and/or velocity measurements. The global properties of all of the outflows in MM1 (e.g., M_{out} , and P_{out}) agree with those derived from CO (1-0) interferometric observations by Shepherd et al. (2007), who treated all outflows in MM1 as a single outflow. Further, the estimated dynamical ages of all outflows suggest that MM1-OF1 is the oldest while the lifetimes of MM1-OF2/OF3/OF4 are comparable, whereas all of the outflows are very young with respect to the average dynamical time of order of 10^4 yr over near 400 molecular outflows catalogued by Wu et al. (2004).

If we assume momentum-driven outflows in protostellar-jet/outflow systems (e.g., Masson & Chernin 1993; Goddi et al. 2020) along with momentum conservation, the relation $\dot{M}_{\text{jet}} V_{\text{jet}} = \dot{M}_{\text{out}} V_{\text{out}} = F_{\text{out}}$ follows, where \dot{M}_{jet} and V_{jet} are the mass-loss rate and the speed of the jet, respectively. The jet speed for massive outflows was observationally measured to be around 500 km s⁻¹ in several proper motion studies of radio continuum jets (e.g., Marti, Rodriguez, & Reipurth 1995). In protostellar jet/outflow systems, the ejection rate is expected to correlate with the accretion rate via the relation $\dot{M}_{\text{acc}} = (1 + f_{\text{jet}}) / f_{\text{jet}} \times \dot{M}_{\text{jet}}$. The fraction f_{jet} , defined as the ratio between the accretion mass rate and the mass-loss rate through the jet, is poorly constrained by observations, but predicted in models to be 0.2–0.5 (e.g., Offner & Arce 2014; Kuiper, Turner, & Yorke 2016). This f_{jet} range yields a range of the mass accretion rates for each outflow (last column of Table 2). If all of the outflows in MM1 are treated as a single entity, the total mass accretion rate onto the protostars will be in the range $[5, 11] \times 10^{-5} M_{\odot}$ yr⁻¹, which is in agreement with rates estimated for other high-mass star-forming systems (e.g., Zhang et al. 2005, 2013; Yuan et al. 2018)

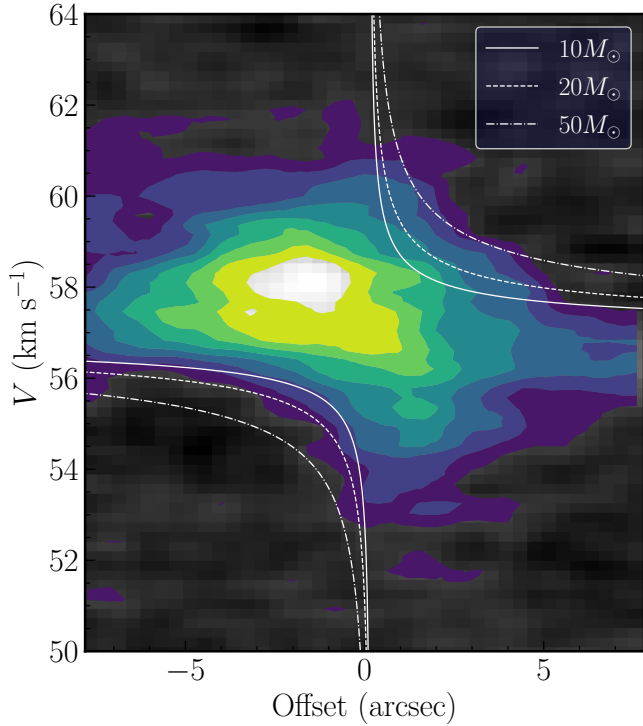


Figure 5. Position velocity diagram of H^{13}CO^+ (1-0) for G34-MM1. The position offset is along the D direction indicated in Fig. 2b. Overlaid on the image are models for Keplerian rotation with central masses of 10, 20, and $50 M_{\odot}$.

3.5 A rotating envelope within MM1?

The extended H^{13}CO^+ emission presents a clear southwest-northeast (SW-NE) velocity gradient (i.e., along the direction D in Fig. 2b), with red-shifted emission to the southwest and blue-shifted emission to the northeast of the MM1-a core. This observed velocity gradient has already been reported in higher $0''.6$ -resolution observations of CH_3OH at ~ 345 GHz with SMA by Rathborne et al. (2011) (see right panel of their Fig. 6). Ruling out the possibility of the influence from the large-scale MM1-OF1 outflow, these authors interpreted the velocity gradient as arising from a rotating structure surrounding the protostar(s) embedded in the core. Note that the SW-NE velocity gradient shown here is seen only in emission of H^{13}CO^+ but not in other species including the complex organic molecules (COMs), such as CH_3OH , which are hot-gas tracers. This could perhaps be attributed to either the different transitions involved or the different spatial resolutions of the two data sets. For example, the transition responsible for CH_3OH emission at ~ 90 GHz in the ATOMS data has a much lower upper energy temperature (~ 20 K) than that of the transition of CH_3OH at ~ 345 GHz where the temperature is > 100 K. The CH_3OH emission at ~ 90 GHz could therefore be tracing different physical regions than those by CH_3OH at ~ 345 GHz. Besides, the resolution of the ATOMS $\sim 2''$ (corresponding to ~ 0.035 pc at the distance of the G34 cloud) is around 3.3 times lower than that of the SMA observations of Rathborne et al. (2011), and hence, the CH_3OH emission of the ATOMS may not be able to resolve the velocity structure at the small-scale, local area of hot gas of around 0.004 pc as revealed in Rathborne et al. (2011).

To better understand the velocity distribution along the direction of the velocity gradient (i.e., direction D in Fig. 2b), we plot the

Table 3. Jeans parameters on cloud and clump scales.

Parameter	Cloud	Clump
$L_{\text{Jeans}}^{\text{th}}$ (pc):	~ 0.1	~ 0.06
$M_{\text{Jeans}}^{\text{th}}$ (M_{\odot}):	~ 2.6	~ 1.9
$L_{\text{Jeans}}^{\text{turb}}$ (pc):	~ 0.4	~ 0.32
$M_{\text{Jeans}}^{\text{turb}}$ (M_{\odot}):	~ 180	~ 130
$L_{\text{frag}}^{\text{ob}}$ (pc):	~ 0.7	~ 0.12
$M_{\text{frag}}^{\text{ob}}$ (M_{\odot}):	$\sim 400\text{--}500$	~ 115

position-velocity diagram in Fig. 5. It reveals a typical butterfly-shaped appearance that is characteristic of Keplerian rotation pattern, which might be another indication of the existence of a rotating envelope. Quantitatively, the velocity pattern can be fitted with a Keplerian rotation curve around an $M \sin^2 \theta \sim 10\text{--}50 M_{\odot}$ protostar, where θ is defined as the inclination angle between the rotation axis and the line of sight. Although this range of masses is consistent with the luminosity ($10^{4.3} L_{\odot}$) and spectral type (B0) determined from the SED of the MM1-a core by Rathborne, Jackson, & Simon (2006), it is still rather small compared with the core's mass ($\sim 200 M_{\odot}$, see Table 1) and is inconsistent with the assumption of the Keplerian rotation that requires the gas mass to be negligible with respect to the central mass (e.g., Cesaroni et al. 2019). This inconsistency can be alleviated if the rotating envelope is sufficiently inclined. For example, if $M \sin^2 \theta \sim 10 M_{\odot}$, the stellar mass can exceed the core mass of $200 M_{\odot}$ for $\theta < 13^{\circ}$.

The mass discrepancy can also be addressed if one considers the mass of $\sim 8 M_{\odot}$ of the more concentrated ~ 0.02 pc diameter core, as defined by Rathborne et al. (2011), rather than the large mass of the MM1-a core ~ 0.04 pc in diameter estimated with the ATOMS data. Even if this is the case, the rotating structure is too large, around $10''$ (0.18 pc), to be arising from an accretion disk, which is generally observed to have a size of a few hundred AUs (e.g., Rathborne et al. 2011; Moscadelli et al. 2021). We therefore suggest that the large-scale velocity-coherent gradient revealed in H^{13}CO^+ emission could be ascribed to a relatively large, rotating structure.

3.6 Virial Analysis

We carry out a virial analysis to assess the gravitational stability of dense cores. Following the framework of Bertoldi & McKee (1992), the virial mass can be defined as

$$M_{\text{vir}} = \frac{5\sigma_{\text{tot}}^2 R_{\text{core}}}{G}, \quad (1)$$

where R_{core} is the core radius, and G is the gravitational constant. Following Eq. 2 of Liu, Stutz, & Yuan (2019), the total velocity dispersion, σ_{tot} , was calculated as $\sigma_{\text{tot}}^2 = \sigma_{\text{th}}^2 + \sigma_{\text{nt}}^2$, to include both thermal and non-thermal support against gravity. In this calculation, the same temperatures as assumed for calculating core masses were taken to be the kinetic temperature of the cores, while the line widths, $\Delta V_{\text{H}^{13}\text{CO}^+}$, derived from the spectrum of H^{13}CO^+ (1-0) averaged over each core (see Table 1) were used for the σ_{nt} estimate. The virial and observed masses can be compared using the virial parameter,

$$\alpha_{\text{vir}} = \frac{M_{\text{vir}}}{M_{\text{core}}} = \frac{5\sigma_{\text{tot}}^2 R_{\text{core}}}{GM_{\text{core}}}. \quad (2)$$

The significance of Eq. 2 is that supercritical cores with $\alpha_{\text{vir}} \leq 2$ will collapse towards star formation, while subcritical cores with $\alpha_{\text{vir}} > 2$ will expand or must be confined by additional forces (e.g.,

magnetic field and/or external pressure, [Kauffmann, Pillai, & Goldsmith 2013](#)). As we see in Table 1, $\alpha_{\text{vir}} < 2$ for all cores, which means that they are most likely gravitationally bound and will evolve to collapse, leading to star formation.

3.7 Jeans length and Jeans mass

Figure 1 clearly shows fragmentation on two different scales of the cloud and clumps. On the cloud scale, the fragmentation proceeds with ~ 0.7 pc-separated fragments of masses 200–500 M_{\odot} (clumps MM1, MM2, and MM4 in Fig. 1a), where the fragment masses are from Table 1 of [Liu et al. \(2020a\)](#) and the fragment separation is the averaged distance between neighbouring clumps. On the core scale, the fragmentation is evidenced by ~ 0.12 pc-separated fragments of typical mass 115 M_{\odot} , where only the fragments (cores) within MM1 are considered, since the population of cores in MM2 suffers from the incomplete coverage in the ATOMS. In this case, the typical mass of the fragments is taken to be the average mass of the cores within MM1, while the typical separation between fragments is determined from the minimum spanning tree technique (e.g., [Dib & Henning 2019](#)), which determines the shortest distances that can possibly connect each of the cores in the sampled field.

To investigate the observed two-scale fragmentation in the G34 cloud we evaluate the Jeans parameters, i.e., Jeans length and Jeans mass, of both cloud and clump scales (e.g., [Wang et al. 2014; Palau et al. 2014](#)):

$$L_{\text{Jeans}} = \sqrt{\frac{\pi c_{\text{eff}}^2}{G \rho_{\text{eff}}}}, \quad (3)$$

and

$$M_{\text{Jeans}} = \frac{\pi^{5/2}}{6 G^{3/2}} c_{\text{eff}}^3 \rho_{\text{eff}}^{-1/2}. \quad (4)$$

where c_{eff} and ρ_{eff} are the effective sound speed, and density, respectively. If thermal support alone is considered, c_{eff} will be the isothermal sound speed (or the thermal velocity dispersion, σ_{th}), and accordingly we obtain the thermal Jeans parameters, $L_{\text{Jeans}}^{\text{th}}$ and $M_{\text{Jeans}}^{\text{th}}$. If both thermal and non-thermal support are involved, c_{eff} will correspond to the total velocity dispersion $\sigma_{\text{tot}} = \sqrt{\sigma_{\text{th}}^2 + \sigma_{\text{nt}}^2}$, yielding the turbulent Jeans parameters, $L_{\text{Jeans}}^{\text{turb}}$ and $M_{\text{Jeans}}^{\text{turb}}$.

For the estimate of Jeans parameters on the cloud scale, we assume a gas kinetic temperature of ~ 21 K, which corresponds to the average dust temperature over the entire cloud region investigated here (see Sect. 3.1), and a line width of $\Delta V_{\text{H}^{13}\text{CO}^+} = 1.3 \text{ km s}^{-1}$, which is a typical value of the weak-feedback cloud area (see Fig. 2c and Sect. 3.2), and thus more representative of the initial turbulence of the cloud than the line widths found in the relatively strong-feedback areas. Following [Liu, Stutz, & Yuan \(2019\)](#), σ_{th} is estimated from the gas kinetic temperature and σ_{nt} is determined from $\Delta V_{\text{H}^{13}\text{CO}^+}$. Finally, using the cloud-average density, $n_{\text{cl}} \sim 2.6 \times 10^5 \text{ cm}^{-3}$ (i.e., $\rho_{\text{eff}}^{\text{cl}} \sim 4.4 \times 10^{-19} \text{ g cm}^{-3}$) both thermal and turbulent Jeans parameters are calculated on the cloud scale. Likewise, both thermal and turbulent Jeans parameters on the clump scale can be estimated assuming the same values of gas temperature and line width values as above. This assumption is valid if both cloud- and clump-scale fragmentation occur sufficiently early that the cloud is free of strong star-formation feedback. In this case, the mean density of the clump, $n_{\text{clump}} \sim 4.9 \times 10^5 \text{ cm}^{-3}$ ([Liu et al. 2020a](#), i.e., $\rho_{\text{eff}}^{\text{clump}} \sim 8.2 \times 10^{-19} \text{ g cm}^{-3}$) is adopted.

Table 3 summarizes the derived Jeans parameters at both cloud and clump scales. At the cloud level fragmentation, the predicted

thermal Jeans length is a factor of ~ 7 smaller than the observed separation of the fragments (clumps) and the thermal Jeans mass is a factor of $\sim 150 - 200$ smaller than the observed masses. In comparison, the turbulent Jeans parameters are closer to the observed values. Now, considering the fragmentation at the clump scale, the typical core separation observed is similar (within a factor of ~ 2) to the predicted Jeans parameters with and without turbulence. In contrast, the predicted thermal Jeans mass is significantly (by a factor of ~ 60) smaller than the observed core masses which are closer to the estimated turbulent Jeans mass. This strongly suggests that the observed hierarchical fragmentation seen at two different spatial scales of the G34 cloud is driven in part by turbulence.

As magnetic fields provide support against gravity, their role in the fragmentation process has been extensively investigated in several theoretical and simulation studies ([Commerçon, Hennebelle, & Henning 2011; Palau et al. 2013](#), and references therein). Recent observations by [Palau et al. \(2021\)](#) of a sample of 18 fragmenting massive cores enable a comprehensive study of fragmentation and magnetic fields, where a tentative correlation between the fragmentation level and the magnetic field strength has been found with stronger magnetic fields corresponding to a less fragmentation level. From thermal dust polarization observations at $350 \mu\text{m}$ within the filamentary G34 cloud, [Tang et al. \(2019\)](#) propose a combination of gravity, turbulence, and magnetic field, with varying degree of contribution, to explain different levels of fragmentation in the associated clumps, MM1, MM2, and MM3. Based on SMA and CARMA observations ([Zhang et al. 2014; Hull et al. 2014](#)), where no smaller scale structures are resolved in MM1, these authors conclude that the absence of observed fragmentation in this clump is due to the dominance of gravity over magnetic field and turbulence which enables a global collapse. In another study, [Soam et al. \(2019\)](#) have mapped the magnetic fields in the G34 cloud at $870 \mu\text{m}$ and estimated the field strength of the MM1 clump to be $\sim 500 \mu\text{G}$, which would dominate given the inferred sub-alfvénic nature of the cloud.

Our ATOMS continuum observations give a new insight into the above processes in MM1 by revealing a cluster of seven cores. In addition to the turbulence driven fragmentation picture observed in G34, the above analysis based on the previous studies suggests that magnetic fields play a decisive role in fragmentation both at the cloud and the clump scale, especially for the fragmentation discerned in the clump MM1. Comparing the distribution of the resolved cores with the orientation of the magnetic field given in [Soam et al. 2019; Tang et al. 2019](#) indicates that fragmentation has ensued mostly along a preferred direction perpendicular to the magnetic field. This agrees well with strong magnetic field cases discussed in [Palau et al. \(2021\)](#).

Additionally, recent statistical studies towards several tens of high-mass star-forming protoclusters or IRDC clumps with interferometric observations down to ~ 1000 AU scales (e.g., [Palau et al. 2013; Beuther et al. 2018; Sanhueza et al. 2019](#)), have revealed large populations of low-mass cores which are consistent with thermal fragmentation. As can be deciphered from these studies and the analysis carried out in this present work, massive fragments (at the scale of clump, cores, or condensations) are additionally supported by turbulence and/or magnetic field where the core/condensations eventually form high-mass stars. In case of small scale condensations, which would either competitively accrete to form high-mass stars or proceed to form the low-mass population of the protocluster, thermal pressure dominates and these are consistent with thermal Jeans fragmentation. Further high-resolution observations of the ATOMS cores would enable us to probe the fragmentation process involved from core to condensation (or star-forming ‘seed’) scales in

the G34 cloud. In this regard, surveys like ALMAGAL hold the potential for in-depth studies of a large sample of similar star-forming regions to gain a better insight into the complex fragmentation processes involved. In summary, while the fragmentation details on the core scales require future in-depth studies, the current observations from the ATOMS suggest that turbulence and magnetic field could act together to drive the fragmentation of both cloud and clump scales.

4 DISCUSSION

4.1 Hierarchical fragmentation

It is widely accepted that hierarchical fragmentation takes place in the star formation process on multiple scales, from molecular cloud to clump, and down to core scales. As shown in Fig. 1, the G34 cloud does present a hierarchical fragmentation scenario with the intermediate-scale clumps fragmented from the large-scale filamentary cloud, followed by the small-scale cores fragmented from the clumps. Moreover, subsequent fragmentation of these detected cores is likely to occur as has been observed towards other star-forming clumps in previous high-resolution observations (e.g., Palau et al. 2013; Beuther et al. 2018), where the fragmentation on core scales into < 1000 AU-size fragments has been revealed.

The observed fragmentation scenario in G34 could favour the hierarchical fragmentation-based models such as the “global hierarchical collapse” and “inertial-inflow” models (Vázquez-Semadeni et al. 2019; Padoan et al. 2020). The former model assumes that fragmentation can occur hierarchically on all scales through the thermal Jeans fragmentation of the relative-scale density structures being in transonic and/or subsonic state. In contrast, the latter model of “inertial-inflow” (Padoan et al. 2020) requires supersonic turbulence to trigger the hierarchical fragmentation, which is consistent with the fragmentation analysis carried out in Sect. 3.7. Certainly, the understanding of the exact driving agents, thermal versus turbulent fragmentation, in the hierarchical fragmentation-based models needs to be constrained in future studies. Moreover, from a theoretical point of view the above models could be complementary to the class of other high-mass star formation models like the “core-accretion” and “competitive accretion” models (McKee & Tan 2003; Bonnell, Vine, & Bate 2004). For example, the “global hierarchical collapse” model claims that the “Bondi-Hoyle” accretion still holds on core scales as predicted by the “competitive accretion” model. To reconcile these two classes of theoretical models requires high-resolution observations of both continuum and lines on multiple scales, i.e., from a few parsecs to a few hundred AUs. This strongly advocates for future higher-resolution, and sufficiently deep observations to scrutinize the core-scale fragmentation process of the G34 cloud.

4.2 Dynamical mass inflow and accretion

The multi-scale, hierarchical fragmentation process could coexist with rich, and characteristic dynamics, such as scale-dependent gas flows and mass accretion (e.g., Peretto et al. 2013; Yuan et al. 2018; Avison et al. 2021; Ren et al. 2021). Such dynamical processes are believed to determine the final mass of the newly-formed stars (e.g., Beuther et al. 2018; Motte, Bontemps, & Louvet 2018; Vázquez-Semadeni et al. 2019; Padoan et al. 2020). Therefore, it is worthwhile to investigate the dynamics of G34 to gain further insight into the fragmentation scenario of the cloud.

On the clump scale, we find from Fig. 2b the evident large-scale

velocity-coherent gradients along several directions, for example A and B, towards the cluster of cores within MM2. These velocity gradients are reliable since they are measured from H^{13}CO^+ (1–0), whose emission has a single-peak spectrum almost everywhere especially for the regions investigated here. They are estimated to be around a few $\text{km s}^{-1} \text{pc}^{-1}$ (see Fig. 3). Both outflowing and inflowing gas can contribute to the apparent velocity-coherent gradients. Moreover, we do not find the outflow signatures (i.e., enhanced, high-speed blue or red-shifted emission) from the visual inspection of the PV diagram of H^{13}CO^+ (1–0) at several particularly selected directions (in Fig. 2b). These results indicate that the relatively optically thin H^{13}CO^+ (1–0) emission is not significantly affected by outflows.

As mentioned in Sect. 3.2, the bright branch of the H^{13}CO^+ emission (see Fig. 2a), being morphologically linked to the cluster of cores in MM2, could be an imprint of ambient gas inflowing onto the cluster due to its strong gravitational attraction. In support of this picture, the imprint of the inflowing ambient gas is suggested by a spoke-like gas streamers converging toward the centre of the cluster in MM2 from N_2H^+ (1–0) emission of the ALMA-IRDC survey (Barnes et al. 2021) that reaches a matching angular resolution to the ATOMS survey. Analysing the N_2H^+ (1–0) gas kinematics towards G34, Tang et al. (2019) have discussed about the presence of a large-scale east-west velocity gradient. At smaller and localized scales towards the MM1/MM2 clumps, close alignment between the local magnetic field orientation is also evident indicating that gravity has aligned the gas flow along the field lines onto the protoclusters MM1/MM2. These results agree well with the observed velocity-coherent gradients illustrated in Fig. 2b.

For a quantitative analysis, we proceed along the lines discussed in Moscadelli et al. (2021) to estimate the mass inflowing rate of the gas flows onto the cluster of cores within both MM1 and MM2. Based on the peak intensity map (see Fig. 2a), we approximately delineate the gas inflow regions with two polygons (see Fig. 2b), each morphologically encompassing the gas emission possibly linked to each cluster of cores. Here, the mass inflowing rate, \dot{M}_{inf} , is calculated from the ratio of the momentum, P_{inf} , to the length, L_{inf} , of the flow, similar to the approach followed in calculating the outflow properties in Sect. 3.4. L_{inf} corresponds to the largest extent of the gas inflowing areas (see Fig. 2b), i.e., $\sim 0.26 \text{ pc}$ and $\sim 0.33 \text{ pc}$ for the cluster of cores in MM1, and MM2, respectively. We assume a clump-averaged abundance of 9×10^{-12} for H^{13}CO^+ (1–0) as estimated in Liu et al. (2020a). The velocities of inflowing gas are in the range [53, 61] km s^{-1} bracketing the systemic velocity of 57.6 km s^{-1} for the individual MM1 system, and 57 km s^{-1} for MM2. Following Sect. 3.4, and confining the analysis to the gas inflowing area for each cluster of cores, we find that the gas could be inflowing onto the cluster of cores in MM1 at $\dot{M}_{\text{inf}} \simeq 2.7 \times 10^{-4} M_{\odot} \text{ yr}^{-1}$, and in MM2 at $\dot{M}_{\text{inf}} \simeq 3.6 \times 10^{-4} M_{\odot} \text{ yr}^{-1}$. These results are in good agreement with those of Moscadelli et al. (2021), who observed the mass inflow rate onto the core cluster to be around $10^{-4} M_{\odot} \text{ yr}^{-1}$ in a high-mass star-forming clump in IRAS 21078+5211. On the core scale, several associated, highly-collimated outflows are found in both clusters of cores. The outflows are generally thought to be an indirect evidence for disk accretion.

\dot{M}_{inf} corresponds to the mass inflow of clump scale gas onto the cores, while \dot{M}_{acc} corresponds to the mass accretion of the core scale onto the stellar disk. It is therefore natural to compare the mass inflow/accretion rates of different scales. We find that $\dot{M}_{\text{inf}} \gg \dot{M}_{\text{acc}}$, suggesting that the mass inflow/accretion rate from the clump to core scales is higher than that from the core to disk scales. While the observed scale-dependent mass inflow/accretion

rates seem to agree well with the “inertial-inflow” model (Padoan et al. 2020), one cannot rule out the “global hierarchical collapse” scenario. In the “inertial-inflow” model, the mass inflow/accretion rate is predicted to be a growing function of distance from the centre of star-forming clusters, so that the large-scale mass inflow rate can control the small-scale mass accretion rate onto the star(s), leading to a cascade of the scale-dependent mass feeding from large to small scales. In comparison, the scenario of the large scale density structures regulating the small-scale structures in dynamical accretions is also predicted in the “global-hierarchical collapse” model which suggests a similar cascade of scale-dependent mass feeding due to the top-down mass accretion process from large to small scales (Vázquez-Semadeni et al. 2019). Therefore, further dedicated dynamics and kinematics analysis in the future remains necessary to distinguish between the two models from an observational point of view.

This cascade of scale-dependent mass feeding scenario has already been demonstrated from observations (e.g., Motte, Bontemps, & Louvet 2018; Yuan et al. 2018; Avison et al. 2021), in which the central protostar, the core, and the clump are found to simultaneously grow in mass via core-fed/disk accretion, clump-fed accretion, and filamentary/cloud-fed accretion respectively, with a trend of increasing mass inflow/accretion rate. This suggests that high-mass star formation could be a dynamical mass inflow/accretion process linked to the multi-scale fragments from the clouds, through clumps and cores, down to seeds or condensations of star formation. We therefore suggest that the high-mass star-forming G34 cloud could be undergoing a multi-scale, and dynamical inflow/accretion process, which could be linked to multi-scale fragmentation.

5 SUMMARY AND CONCLUSIONS

We have presented new observations of 3 mm continuum and molecular transitions (e.g., $\text{HCO}^+/\text{H}^{13}\text{CO}^+$ $J = 1-0$, and $\text{CS } J = 2-1$ from the ATOMS survey) for tracing both dense gas and outflows in the two massive protostellar clumps, MM1 and MM2, in the G34 filamentary IRDC cloud. We have analyzed the fragmentation and dynamics of the cloud down to the cores of ~ 0.03 pc in radius, and our main results are the following:

- Nine dust cores have been extracted from 3 mm dust continuum emission: seven within the MM1 clump and two within MM2. The seven cores represent the most complete population of cores unveiled so far for MM1, while the small population of only two detected cores in MM2 is mainly attributed to the incomplete coverage by the ATOMS survey.

- The nine cores have median radius 0.03 pc (range 0.02–0.04 pc), median mass $115 M_\odot$ (range $\sim 40\text{--}280 M_\odot$), median number density $1.1 \times 10^7 \text{ cm}^{-3}$ (range $0.2 \times 10^7\text{--}2.8 \times 10^7 \text{ cm}^{-3}$), and median mass surface density 11 g cm^{-2} (range $\sim 2\text{--}33 \text{ g cm}^{-2}$). All of the cores have virial parameter $\alpha_{\text{vir}} < 2$, suggesting that they are most likely gravitationally bound and will proceed towards the formation of new stars.

- The identification of new outflows suggests the presence of at least four individual, highly-collimated outflows within MM1 as opposed to the two wide-angle outflows reported in Shepherd et al. (2007). The outflow properties in MM1 are confirmed to be attributed to a B0-type star with a total outflowing mass of $\sim 45 M_\odot$, and total energy of $\sim 1 \times 10^{47}$ ergs. Additionally, a total mass accretion rate onto the protostars in MM1, \dot{M}_{acc} , is estimated to be of the order of $10^{-5} M_\odot \text{ yr}^{-1}$ in the framework of momentum con-

servation between mass inflow and momentum-driven outflows in a protostellar-jet/outflow system.

- A large-scale, butterfly-shaped velocity gradient pattern is observed in H^{13}CO^+ (1–0) emission surrounding the MM1-a core, which is consistent with the picture revealed in CH_3OH at 345 GHz by Rathborne et al. 2011. The large-scale nature of the pattern (size ~ 0.18 pc) suggests that the observed velocity gradient could arise from a large, rotating structure rather than from a small, rotating disk.

- Two-scale hierarchical fragmentation is evident on both cloud and clump scales. It could be driven by a combination of the initial turbulence and magnetic field on both scales. With the potential of the cores to fragment further into star formation seeds of sizes $< \sim 1000$ AU, we assume that a multi-scale, hierarchical fragmentation process is at work in the G34 cloud.

- Intermediate-scale velocity gradients towards each cluster of cores are found in both MM1 and MM2 clumps with a typical amplitude of $3\text{--}8 \text{ km s}^{-1} \text{ pc}^{-1}$. These are interpreted as the gas inflowing onto the cluster in the context of the multi-scale, hierarchical fragmentation. The corresponding mass inflow rate, \dot{M}_{inf} , is estimated to be of order of $10^{-4} M_\odot \text{ yr}^{-1}$.

- \dot{M}_{acc} responsible for the small-scale mass accretion from cores onto protostars and disks is found to be lower than \dot{M}_{inf} for the larger-scale mass inflow from clumps onto the cluster of cores. This difference suggests a scale-dependent inflow/accretion cascade scenario from large to small scales, which could be linked to the multi-scale fragmentation process.

Multi-scale fragmentation from clouds, through clumps and cores, down to seeds of star formation and the cascade of scale-dependent mass inflow/accretion observed in G34 allow us to conclude that the cloud is undergoing a dynamical mass inflow/accretion process. Confirmation of this process would support hierarchical fragmentation-based models, e.g., “global hierarchical collapse” and “inertial-inflow” models.

Acknowledgements

We thank the anonymous referee for comments and suggestions that greatly improved the quality of this paper. Tie Liu acknowledges the supports by National Natural Science Foundation of China (NSFC) through grants No.12073061 and No.12122307, the international partnership program of Chinese academy of sciences through grant No.114231KYSB20200009, and Shanghai Pujiang Program 20PJ1415500. This research was carried out in part at the Jet Propulsion Laboratory, which is operated by the California Institute of Technology under a contract with the National Aeronautics and Space Administration (80NM0018D0004). S.-L. Qin is supported by NSFC under No.12033005. L.B. and A.S. acknowledge support from CONICYT project Basal AFB-170002. AS gratefully acknowledges funding support through Fondecyt Regular (project code 1180350). C.W.L. is supported by Basic Science Research Program through the National Research Foundation of Korea (NRF) funded by the Ministry of Education, Science and Technology (NRF-2019R1A2C1010851). This paper makes use of the following ALMA data: ADS/JAO.ALMA#2019.1.00685.S. ALMA is a partnership of ESO (representing its member states), NSF (USA), and NINS (Japan), together with NRC (Canada), MOST and ASIAA (Taiwan), and KASI (Republic of Korea), in cooperation with the Republic of Chile. The Joint ALMA Observatory is operated by ESO, AUI/NRAO, and NAOJ. This research made use of astrodendro, a Python package to compute dendrograms of Astronomical data (<http://www.dendrograms.org/>). This research made

use of Astropy, a community-developed core Python package for Astronomy (Astropy Collaboration, 2018).

Data availability

The data underlying this article are available in the article and in its online supplementary material.

REFERENCES

- Arce H. G., Shepherd D., Gueth F., Lee C.-F., Bachiller R., Rosen A., Beuther H., 2007, *prpl.conf*, 245
- Avison A., Fuller G. A., Peretto N., Duarte-Cabral A., Rosen A. L., Traficante A., Pineda J. E., et al., 2021, *A&A*, 645, A142. doi:10.1051/0004-6361/201936043
- Barnes A. T., Henshaw J. D., Fontani F., Pineda J. E., Cosentino G., Tan J. C., Caselli P., et al., 2021, *MNRAS*, 503, 4601. doi:10.1093/mnras/stab803
- Beltrán M. T., Rivilla V. M., Cesaroni R., Maud L. T., Galli D., Moscadelli L., Lorenzani A., et al., 2021, *A&A*, 648, A100. doi:10.1051/0004-6361/202040121
- Bertoldi F., McKee C. F., 1992, *ApJ*, 395, 140. doi:10.1086/171638
- Beuther H., Mottram J. C., Ahmadi A., Bosco F., Linz H., Henning T., Klaassen P., et al., 2018, *A&A*, 617, A100. doi:10.1051/0004-6361/201833021
- Bonnell I. A., Vine S. G., Bate M. R., 2004, *MNRAS*, 349, 735. doi:10.1111/j.1365-2966.2004.07543.x
- Bronfman L., Nyman L.-A., May J., 1996, *A&AS*, 115, 81
- Carey S. J., Clark F. O., Egan M. P., Price S. D., Shipman R. F., Kuchar T. A., 1998, *ApJ*, 508, 721. doi:10.1086/306438
- Carey S. J., Feldman P. A., Redman R. O., Egan M. P., MacLeod J. M., Price S. D., 2000, *ApJL*, 543, L157. doi:10.1086/317270
- Cesaroni R., Hofner P., Araya E., Kurtz S., 2010, *A&A*, 509, A50. doi:10.1051/0004-6361/200912877
- Cesaroni R., Beuther H., Ahmadi A., Beltrán M. T., Csengeri T., Galván-Madrid R., Gieser C., et al., 2019, *A&A*, 627, A68. doi:10.1051/0004-6361/201935506
- Chen X., Ren Z., Zhang Q., Shen Z., Qiu K., 2017, *arXiv*, arXiv:1701.02871
- Commerçon B., Hennebelle P., Henning T., 2011, *ApJL*, 742, L9. doi:10.1088/2041-8205/742/1/L9
- Csengeri T., Bontemps S., Wyrowski F., Motte F., Menten K. M., Beuther H., Bronfman L., et al., 2017, *A&A*, 600, L10. doi:10.1051/0004-6361/201629754
- Dib S., Henning T., 2019, *A&A*, 629, A135. doi:10.1051/0004-6361/201834080
- Draine B. T., 2011, *piim.book*
- Goddi C., Ginsburg A., Maud L. T., Zhang Q., Zapata L. A., 2020, *ApJ*, 905, 25. doi:10.3847/1538-4357/abc88e
- Faúndez S., Bronfman L., Garay G., Chini R., Nyman L.-A., May J., 2004, *A&A*, 426, 97. doi:10.1051/0004-6361/20035755
- Hull C. L. H., Plambeck R. L., Kwon W., Bower G. C., Carpenter J. M., Crutcher R. M., Fiege J. D., et al., 2014, *ApJS*, 213, 13. doi:10.1088/0067-0049/213/1/13
- Isequilla N. L., Ortega M. E., Areal M. B., Paron S., 2021, *arXiv*, arXiv:2103.04965
- Kauffmann J., Pillai T., Goldsmith P. F., 2013, *ApJ*, 779, 185. doi:10.1088/0004-637X/779/2/185
- Kennicutt R. C., 2005, *IAUS*, 227, 3. doi:10.1017/S1743921305004308
- Krumholz M. R., McKee C. F., 2008, *Natur*, 451, 1082. doi:10.1038/nature06620
- Kuiper R., Turner N. J., Yorke H. W., 2016, *ApJ*, 832, 40. doi:10.3847/0004-637X/832/1/40
- Liu H.-L., Sanhueza P., Liu T., Zavagno A., Tang X.-D., Wu Y., Zhang S., 2020a, *ApJ*, 901, 31. doi:10.3847/1538-4357/abadfe
- Liu H.-L., Stutz A., Yuan J.-H., 2019, *MNRAS*, 487, 1259. doi:10.1093/mnras/stz1340
- Liu H.-L., Liu T., Evans N. J., Wang K., Garay G., Qin S.-L., Li S., et al., 2021, *MNRAS.tmp*. doi:10.1093/mnras/stab1352
- Liu T., Evans N. J., Kim K.-T., Goldsmith P. F., Liu S.-Y., Zhang Q., Tatematsu K., et al., 2020b, *MNRAS*, 496, 2821b. doi:10.1093/mnras/staa1501
- Liu T., Evans N. J., Kim K.-T., Goldsmith P. F., Liu S.-Y., Zhang Q., Tatematsu K., et al., 2020c, *MNRAS*, 496, 2790c. doi:10.1093/mnras/staa1577
- Li S., Zhang Q., Pillai T., Stephens I. W., Wang J., Li F., 2019, *ApJ*, 886, 130. doi:10.3847/1538-4357/ab464e
- Li S., Zhang Q., Liu H. B., Beuther H., Palau A., Girart J. M., Smith H., et al., 2020, *ApJ*, 896, 110. doi:10.3847/1538-4357/ab84f1
- Lu X., Zhang Q., Liu H. B., Wang J., Gu Q., 2014, *ApJ*, 790, 84. doi:10.1088/0004-637X/790/2/84
- Marsh K. A., Whitworth A. P., Lomax O., Ragan S. E., Becciani U., Cambrésy L., Di Giorgio A., et al., 2017, *MNRAS*, 471, 2730. doi:10.1093/mnras/stx1723
- Martí J., Rodríguez L. F., Reipurth B., 1995, *ApJ*, 449, 184. doi:10.1086/176044
- Masson C. R., Chernin L. M., 1993, *ApJ*, 414, 230. doi:10.1086/173071
- McKee C. F., Tan J. C., 2003, *ApJ*, 585, 850. doi:10.1086/346149
- McMullin J. P., Waters B., Schiebel D., Young W., Golap K., 2007, *ASPC*, 376, 127
- Moscadelli L., Beuther H., Ahmadi A., Gieser C., Massi F., Cesaroni R., Sánchez-Monge Á., et al., 2021, *A&A*, 647, A114. doi:10.1051/0004-6361/202039837
- Motte F., Bontemps S., Louvet F., 2018, *ARA&A*, 56, 41. doi:10.1146/annurev-astro-091916-055235
- Offner S. S. R., Arce H. G., 2014, *ApJ*, 784, 61. doi:10.1088/0004-637X/784/1/61
- Padoan P., Pan L., Juvela M., Haugbølle T., Nordlund Å., 2020, *ApJ*, 900, 82. doi:10.3847/1538-4357/abaa47
- Palau A., Fuente A., Girart J. M., Estalella R., Ho P. T. P., Sánchez-Monge Á., Fontani F., et al., 2013, *ApJ*, 762, 120. doi:10.1088/0004-637X/762/2/120
- Palau A., Estalella R., Girart J. M., Fuente A., Fontani F., Commerçon B., Busquet G., et al., 2014, *ApJ*, 785, 42. doi:10.1088/0004-637X/785/1/42
- Palau A., Zhang Q., Girart J. M., Liu J., Rao R., Koch P. M., Estalella R., et al., 2021, *ApJ*, 912, 159. doi:10.3847/1538-4357/abee1e
- Peretto N., Fuller G. A., Duarte-Cabral A., Avison A., Hennebelle P., Pineda J. E., André P., et al., 2013, *A&A*, 555, A112. doi:10.1051/0004-6361/201321318
- Peters T., Zhukovska S., Naab T., Girichidis P., Walch S., Glover S. C. O., Klessen R. S., et al., 2017, *MNRAS*, 467, 4322. doi:10.1093/mnras/stx341
- Pillai T., Kauffmann J., Wyrowski F., Hatchell J., Gibb A. G., Thompson M. A., 2011, *A&A*, 530, A118. doi:10.1051/0004-6361/201015899
- Rathborne J. M., Jackson J. M., Chambers E. T., Simon R., Shipman R., Frieswijk W., 2005, *ApJL*, 630, L181. doi:10.1086/491656
- Rathborne J. M., Jackson J. M., Simon R., 2006, *ApJ*, 641, 389. doi:10.1086/500423
- Rathborne J. M., Garay G., Jackson J. M., Longmore S., Zhang Q., Simon R., 2011, *ApJ*, 741, 120. doi:10.1088/0004-637X/741/2/120
- Reid M. J., Menten K. M., Brunthaler A., Zheng X. W., Dame T. M., Xu Y., Wu Y., et al., 2014, *ApJ*, 783, 130. doi:10.1088/0004-637X/783/2/130
- Reid M. J., Menten K. M., Brunthaler A., Zheng X. W., Dame T. M., Xu Y., Li J., et al., 2019, *ApJ*, 885, 131. doi:10.3847/1538-4357/ab4a11
- Ren Z., Zhu L., Shi H., Yue N., Li D., Zhang Q., Mardones D., et al., 2021, *arXiv*, arXiv:2105.04116
- Rosero V., Hofner P., Claussen M., Kurtz S., Cesaroni R., Araya E. D., Carrasco-González C., et al., 2016, *ApJS*, 227, 25. doi:10.3847/1538-4365/227/2/25
- Sakai T., Sakai N., Foster J. B., Sanhueza P., Jackson J. M., Kassis M., Furuya K., et al., 2013, *ApJL*, 775, L31. doi:10.1088/2041-8205/775/1/L31
- Sanhueza P., Contreras Y., Wu B., Jackson J. M., Guzmán A. E., Zhang Q., Li S., et al., 2019, *ApJ*, 886, 102. doi:10.3847/1538-4357/ab45e9
- Shepherd D. S., Povich M. S., Whitney B. A., Robitaille T. P., Nürnberger D. E. A., Bronfman L., Stark D. P., et al., 2007, *ApJ*, 669, 464. doi:10.1086/521331
- Shepherd D. S., Nürnberger D. E. A., Bronfman L., 2004, *ApJ*, 602, 850. doi:10.1086/381050
- Soam A., Liu T., Andersson B.-G., Lee C. W., Liu J., Juvela M., Li P. S., et al., 2019, *ApJ*, 883, 95. doi:10.3847/1538-4357/ab39dd
- Svoboda B. E., Shirley Y. L., Traficante A., Battersby C., Fuller G. A.,

- Zhang Q., Beuther H., et al., 2019, *ApJ*, 886, 36. doi:10.3847/1538-4357/ab40ca
- Tan J. C., Beltrán M. T., Caselli P., Fontani F., Fuente A., Krumholz M. R., McKee C. F., et al., 2014, *prpl.conf*, 149. doi:10.2458/azu.uapress_9780816531240-ch007
- Tang Y.-W., Koch P. M., Peretto N., Novak G., Duarte-Cabral A., Chapman N. L., Hsieh P.-Y., et al., 2019, *ApJ*, 878, 10. doi:10.3847/1538-4357/ab1484
- Urquhart J. S., Thompson M. A., Moore T. J. T., Purcell C. R., Hoare M. G., Schuller F., Wyrowski F., et al., 2013, *MNRAS*, 435, 400. doi:10.1093/mnras/stt1310
- Vázquez-Semadeni E., Palau A., Ballesteros-Paredes J., Gómez G. C., Zamora-Avilés M., 2019, *MNRAS*, 490, 3061. doi:10.1093/mnras/stz2736
- Wang K., Zhang Q., Wu Y., Zhang H., 2011, *ApJ*, 735, 64. doi:10.1088/0004-637X/735/1/64
- Wang K., Zhang Q., Testi L., van der Tak F., Wu Y., Zhang H., Pillai T., et al., 2014, *MNRAS*, 439, 3275. doi:10.1093/mnras/stu127
- Wenger T. V., Balser D. S., Anderson L. D., Bania T. M., 2018, *ApJ*, 856, 52. doi:10.3847/1538-4357/aaac8
- Wu Y., Wei Y., Zhao M., Shi Y., Yu W., Qin S., Huang M., 2004, *A&A*, 426, 503. doi:10.1051/0004-6361:20035767
- Xu J.-L., Li D., Zhang C.-P., Liu X.-L., Wang J.-J., Ning C.-C., Ju B.-G., 2016, *ApJ*, 819, 117. doi:10.3847/0004-637X/819/2/117
- Yuan J., Li J.-Z., Wu Y., Ellingsen S. P., Henkel C., Wang K., Liu T., et al., 2018, *ApJ*, 852, 12. doi:10.3847/1538-4357/aa9d40
- Zhang Q., Hunter T. R., Brand J., Sridharan T. K., Cesaroni R., Molinari S., Wang J., et al., 2005, *ApJ*, 625, 864. doi:10.1086/429660
- Zhang Q., Wang K., 2011, *ApJ*, 733, 26. doi:10.1088/0004-637X/733/1/26
- Zhang Q., Wang Y., Pillai T., Rathborne J., 2009, *ApJ*, 696, 268. doi:10.1088/0004-637X/696/1/268
- Zhang Q., Qiu K., Girart J. M., Liu H. B., Tang Y.-W., Koch P. M., Li Z.-Y., et al., 2014, *ApJ*, 792, 116. doi:10.1088/0004-637X/792/2/116
- Zhang Y., Tan J. C., De Buizer J. M., Sandell G., Beltran M. T., Churchwell E., McKee C. F., et al., 2013, *ApJ*, 767, 58. doi:10.1088/0004-637X/767/1/58
- Zinnecker H., Yorke H. W., 2007, *ARA&A*, 45, 481. doi:10.1146/annurev.astro.44.051905.092549
- ⁹Department of Astronomy, Peking University, 100871, Beijing, People's Republic of China
- ¹⁰Korea Astronomy and Space Science Institute, 776 Daedeok-daero, Yuseong-gu, Daejeon 34055, Republic of Korea
- ¹¹SOFIA Science Centre, USRA, NASA Ames Research Centre, MS-12, N232, Moffett Field, CA 94035, USA
- ¹²Physical Research Laboratory, Navrangpura, Ahmedabad380 009, India
- ¹³University of Science and Technology, Korea (UST), 217 Gajeong-ro, Yuseong-gu, Daejeon 34113, Republic of Korea
- ¹⁴Astronomy Department, University of California, Berkeley, CA 94720, USA
- ¹⁵School of Physics and Astronomy, Sun Yat-sen University, 2 Daxue Road, Zhuhai, Guangdong, 519082, People's Republic of China
- ¹⁶National Astronomical Observatories, Chinese Academy of Sciences, Beijing 100101, China
- ¹⁷Department of Physics, P.O. box 64, FI-00014, University of Helsinki, Finland
- ¹⁸Departamento de Astronomía, Universidad de Chile, Las Condes, Santiago, Chile
- ¹⁹National Astronomical Observatory of Japan, National Institutes of Natural Sciences, 2-21-1 Osawa, Mitaka, Tokyo 181-8588, Japan
- ²⁰Center for Astrophysics, GuangZhou University, Guangzhou, China
- ²¹University of Chinese Academy of Sciences, Beijing 100049, China
- ²²NAOC-UKZN Computational Astrophysics Centre, University of KwaZulu-Natal, Durban 4000, South Africa
- ²³Departamento de Astronomía, Universidad de Concepción, Av. Esteban Iturra s/n, Distrito Universitario, 160-C, Chile
- ²⁴Max-Planck-Institute for Astronomy, Königstuhl 17, 69117 Heidelberg, Germany
- ²⁵Eötvös Loránd University, Department of Astronomy, Pázmány Péter sétány 1/A, H-1117, Budapest, Hungary
- ²⁶Department of Physics, Taiyuan Normal University, Jinzhong 030619, China
- ²⁷Satyendra Nath Bose National Centre for Basic Sciences, Block-JD, Sector-III, Salt Lake, Kolkata-700 106
- ²⁸Indian Institute of Science Education and Research Tirupati, Rami Reddy Nagar, Karakambadi Road, Mangalam (P.O.), Tirupati 517 507, India

APPENDIX A: OUTFLOWS SEEN IN OTHER MOLECULES

Author affiliations:

- ¹Department of Astronomy, Yunnan University, Kunming, 650091, PR China
- ²Indian Institute of Space Science and Technology, Thiruvananthapuram 695 547, Kerala, India
- ³Shanghai Astronomical Observatory, Chinese Academy of Sciences, 80 Nandan Road, Shanghai 200030, Peoples Republic of China
- ⁴Key Laboratory for Research in Galaxies and Cosmology, Shanghai Astronomical Observatory, Chinese Academy of Sciences, 80 Nandan Road, Shanghai 200030, Peoples Republic of China
- ⁵Jet Propulsion Laboratory, California Institute of Technology, 4800 Oak Grove Drive, Pasadena, CA 91109, USA
- ⁶Key Laboratory of Radio Astronomy, Chinese Academy of Sciences, Nanjing 210008, People's Republic of China
- ⁷Center for Astrophysics | Harvard & Smithsonian, 60 Garden Street, Cambridge, MA 02138, USA
- ⁸Kavli Institute for Astronomy and Astrophysics, Peking University, 5 Yiheyuan Road, Haidian District, Beijing 100871, People's Republic of China

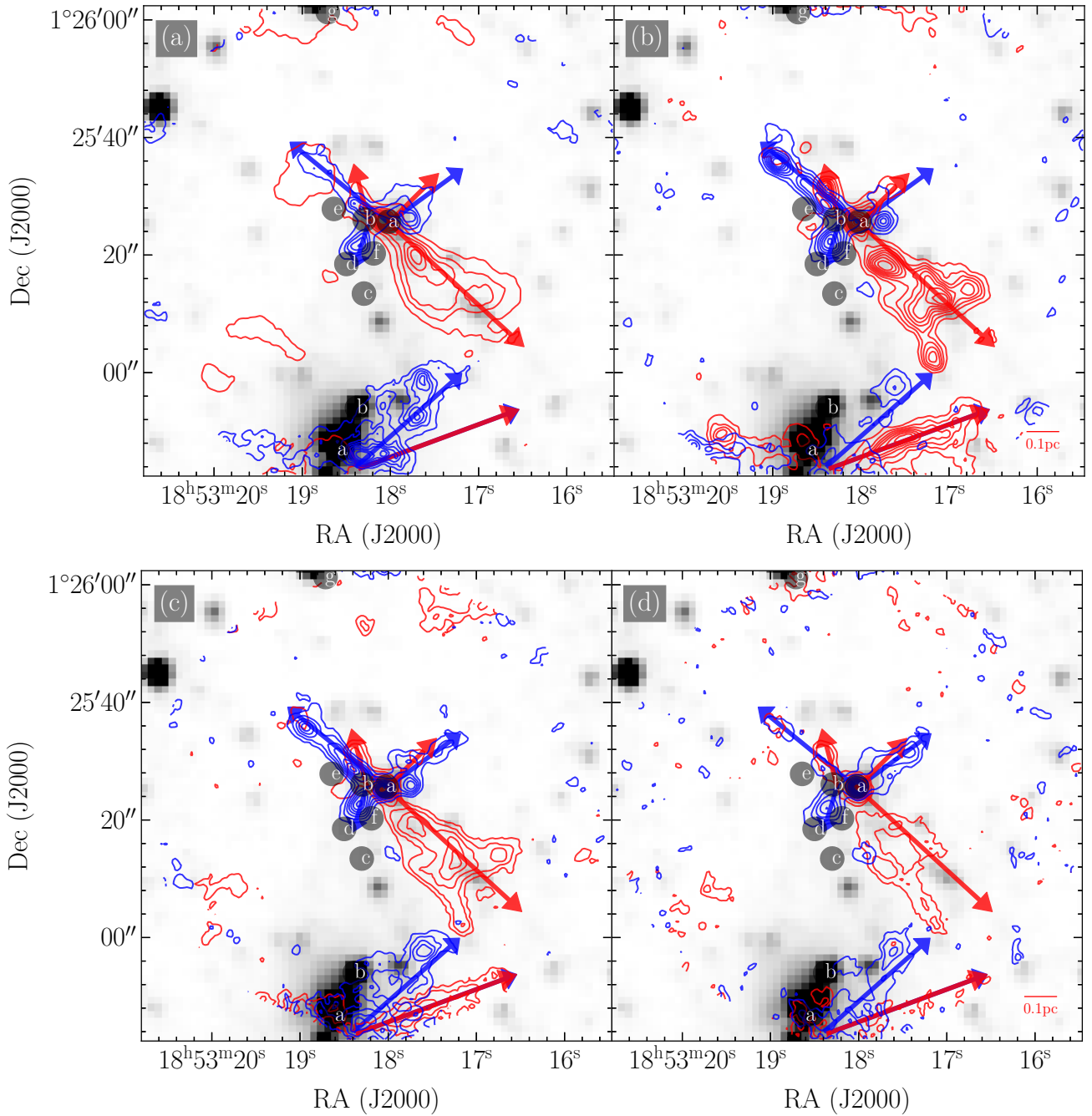


Figure A1. Outflow emission traced by different tracers overlaid on the *Spitzer* 4.5 μm image. Blue- and red-shifted outflowing gas emission in order is integrated over [44.0, 55.0] km s^{-1} and [60.0, 76.0] km s^{-1} for HCO^+ (1-0) in panel a, [42.0, 51.3] km s^{-1} and [63.5, 74.0] km s^{-1} for SiO in panel b, [42.0, 52.7] km s^{-1} and [62.2, 78.0] km s^{-1} for SO in panel c, and [46.0, 54.2] km s^{-1} and [60.6, 66.0] km s^{-1} for CH_3OH in panel d. Labels a–g identify the dense cores in both MM1 and MM2 protostellar clumps. The red and blue arrows correspond to the axes of the CS (2-1) outflow lobes.